Towards a quantified predictive texture classification framework for chromitite breakage behaviour

Nke, A., Chetty, D[1]., Mashaba, D., Govender, V. and Nkwanyana, S.

Mintek, Randburg, South Africa; [1]corresponding author: deshc@mintek.co.za

ABSTRACT

Quantitative texture descriptors may help explain comminution behaviour beyond bulk mineral composition and mineral-scale measurements. This study investigated associations between micro-XRF-derived textural descriptors and t_{10} breakage response in Bushveld Complex chromitite. An established unsupervised framework was applied to 240 drill-core pieces from the Upper Group and Middle Group chromitite layers. Four local textural motif proportions described a continuum of sample textures but did not clearly distinguish samples by t_{10}. An area-weighted textural complexity descriptor showed a negative association with t_{10} in eight selected MG3 samples (Spearman's $\rho = -0.83$, $p = 0.010$), with a weaker association across all 32 t_{10}-tested samples ($\rho = -0.38$, $p = 0.030$). MLA analysis of progeny from eight samples revealed systematic differences in grain shape: exposed chromite grains were generally more angular than enclosed grains, whereas exposed silicate grains were less angular. The latter pattern is consistent with the hypothesis that breakage may follow textural-domain boundaries, including the margins of silicate-rich oikocrysts, rather than exclusively following mineral grain boundaries. However, fracture paths were not directly observed. Spatial textural complexity and grain morphology warrant further investigation using independent samples and registered pre- and post-breakage imaging.

1. INTRODUCTION

Ore texture commonly refers to volume, grain size, shape, spatial distribution and association of each mineral in the ore, i.e., *in situ* (Parian et al., 2018). Ore texture is typically qualitatively described in petrographic terminology, e.g., euhedral, interstitial, laminae, etc., with some terminology specific to rock types and their genesis. In bridging the divide between traditional petrography and process mineralogy, such metrics as mineral abundance, grain size distribution, association, grain shape and added liberation for particulate ore are routinely quantitatively determined from automated microscopy

systems. These attributes are regularly used in geometallurgical work that seeks to link liberation to comminution energies and efficiencies for ore-specific processing.

Standard automated mineralogy routines, however, do not generally provide overarching texture descriptors, which are often developed separately for specific ore types (e.g., Lund et al., 2015). Quantitative texture descriptors are also less commonly applied at centimetre scales, where individual mineral grains may not be resolved. Although several imaging and analysis methods have been developed for geometallurgical applications, no widely adopted framework for quantitative texture characterisation appears to be in use (Månbro et al., 2025; Donskoi et al., 2008; Nguyen et al., 2021; Pérez-Barnuevo et al., 2018; Koch et al., 2019; Becker et al., 2016; Guntoro et al., 2020).

Quantifying texture at this larger scale may help explain differences in breakage response that are not captured by bulk mineral composition or conventional grain-scale measurements alone. One hypothesis is that fractures may preferentially follow boundaries between textural domains, rather than exclusively following individual mineral grain boundaries. Testing this hypothesis requires texture descriptors that capture not only the types and proportions of local motifs, but also the spatial organisation and shape of textural regions.

In this study, chromitite drill-core samples from the Middle Group 3 (MG3) and Upper Group 1 (UG1) horizons of the Bushveld Complex were characterised using micro-XRF imaging and an established unsupervised textural quantification framework. Additional spatial descriptors were evaluated alongside motif proportions to explore their associations with t_{10} breakage response. Progeny from eight selected MG3 samples were also analysed using automated scanning electron microscopy (MLA) to characterise liberation, particle locking and grain morphology. The study provides an exploratory assessment of whether spatial textural descriptors offer complementary information about chromitite breakage and whether post-breakage grain-shape patterns are consistent with the hypothesis of textural-domain-controlled fracture.

2. MATERIALS AND METHODS

2.1. Samples and micro-XRF textural characterisation

Approximately 240 pieces of quartered NQ drill core from the UG1 and MG3 chromitite horizons of the Bushveld Complex were prepared and imaged using a Bruker M4 TORNADO micro-XRF system. For each elemental map, the region of interest, ROI, was defined as the largest rectangle contained within the sample boundary, with its long axis aligned with the drill-core axis. The resulting data were resampled to a common grid with a spatial resolution of 100 µm per pixel.

The seven-stage framework described by Nke et al. (2026) was fitted using a 170-piece development set and subsequently applied unchanged to the samples investigated in the present study (Figure 1). The workflow includes segmentation into chemically coherent textural regions, empirical end-member extraction, non-negative least-squares (NNLS) mineral-affinity classification, calculation of region-level metrics, texton-based motif identification, and representation of samples using motif-proportion histograms. Framework validation combined MLA-based mineral-affinity checks, sample-blocked prediction-strength and bootstrap-resampling tests of motif reproducibility and held-out-sample application of the fitted pipeline to confirm reproducibility. Detailed descriptions of the image processing, segmentation and motif-identification procedures are provided in the companion study.

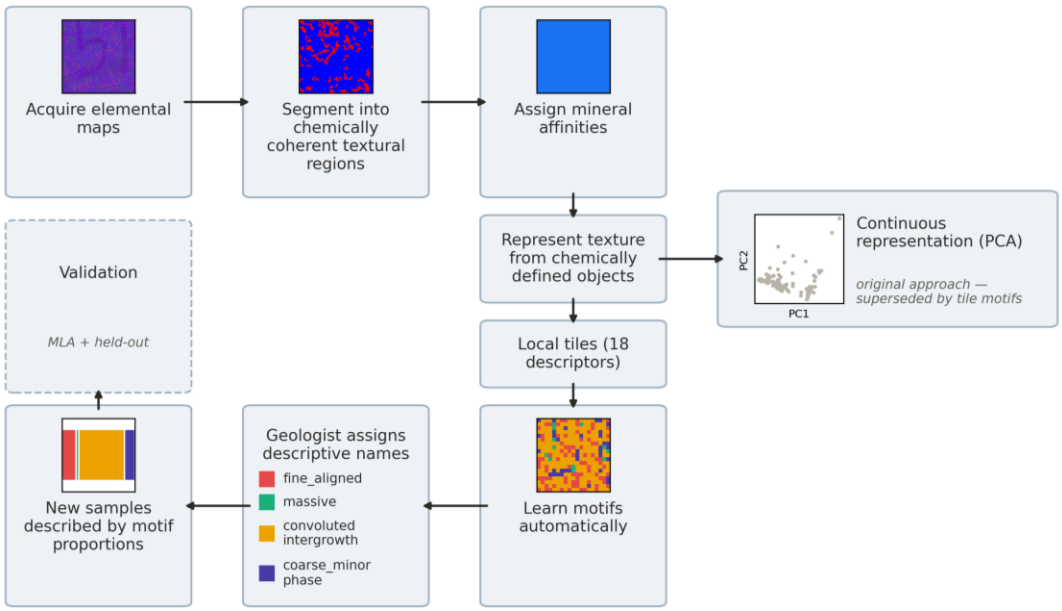

***Figure 1**: Steps in the developed quantitative texture classification framework, from micro-XRF data acquisition, to segmentation, mineral affinity classification, motif discovery, texture quantification and sample texture classification (After Nke et al., 2026)*

The four motifs identified by the framework were retained as established local textural categories, and their areal proportions were used to describe the textural composition of each sample. No additional discrete sample-level texture classes were imposed, as four unsupervised clustering methods (K-means, HDBSCAN, agglomerative hierarchical clustering, and Gaussian mixture models (GMM)) consistently indicated that sample-level textures formed a continuum rather than distinct groups.

2.2. Comminution testing and sample selection

Thirty-two imaged pieces, ~26–30 mm in size, underwent SAG Mill Comminution (SMC®) testing using a consistent test protocol and a specific energy of 1.00 kWh/t. The t_{10} was determined from the mass percentage of progeny passing one-tenth of the original particle size, using a screening threshold of approximately 2.36 mm. Material coarser than this threshold (the +2.36 mm fraction) therefore falls outside the t_{10} definition.

Eight of the 32 MG3 samples were selected for the present study according to their derived t_{10} values. The selection covered the observed range of 61.4–82.6% and included four samples in a high-t_{10} group (78.3–82.6%) and four in a low-t_{10} group (61.4–63.6%). The selection was based on t_{10} rank rather than a combination of comminution indices.

Following SMC testing, progeny from the eight selected samples were sieved into five size fractions: +2.36 mm, -2.36 + 1.18 mm, -1.18 mm + 425 µm, -425 + 212 µm, and -212 µm. Each fraction was mounted, polished, and analysed using a Field Emission Gun (FEG) Mineral Liberation Analyser (MLA) 650F system. Particle- and grain-level data were exported using MLA Dataview and processed in Python.

The eight samples were selected to investigate textural and mineralogical characteristics across a broad range of derived t_{10} values. Consequently, the dataset was not designed to provide an unbiased estimate of the relationship between texture and comminution response across the wider chromitite population.

2.3. Spatial descriptors derived from micro-XRF segmentation

In addition to the proportions of the four textural motifs, three sample-level descriptors were investigated to capture spatial characteristics that motif proportions alone may not represent: region-size distribution, textural complexity and connectivity. These descriptors were derived from the canonical textural regions identified by the established micro-XRF framework and were explored as complementary measures of sample texture.

Region-size distribution described the relative areas occupied by the canonical textural regions. Textural complexity was quantified using the isoperimetric ratio:

$$P^2/(4\pi A)$$

where (P) is the perimeter and (A) is the area of an individual connected region. If a canonical textural region occurred in several disconnected locations, the ratio was calculated separately for each connected occurrence. The median ratio was then calculated for each canonical textural region, and these medians were averaged across the sample, weighted by the total area occupied by each canonical region. This descriptor

quantifies the shape complexity of the connected regions; it does not directly measure fracture alignment with textural boundaries.

Connectivity was calculated for each canonical textural region as the fraction of its total area contained in its largest connected component. The sample-level descriptor was the area-weighted average of these fractions.

Associations between the descriptors and t_{10} were examined using Spearman's rank correlation and leave-one-out sensitivity analysis. These analyses were exploratory and were used to assess the strength and sensitivity of observed associations, rather than to establish predictive performance or a causal breakage mechanism.

2.4. MLA-derived mineralogical and textural measurements

MLA-derived measurements were used to characterise the mineralogical properties of the post-breakage progeny. The analysis considered liberation, grain size, mineral locking complexity, the distribution of hydrous-silicate alteration phases and grain morphology.

MLA analysis was performed the Grain Based Extended Mapping (GXMAP) measurement mode, the MLA generated an X-ray analysis for each grey-level region within a particle (Lotter et al., 2003; Fandrich et al, 2007). This measurement mode was selected based on the ore type, particle size, and its ability to delineate mineral particle and grain boundaries within particles. During the investigation, more than 5,000 particles per polished section for each sample were analysed and processed. Particle and grain properties, including mineral types and compositions, particle size, grain size, density, weight percentage of the particle population, particle area and the perimeter of each particle, were determined during offline processing.

Liberation was assessed using the proportion of grains exposed at the external particle boundary, based on MLA's Free Surface% descriptor. Grains with Free Surface% greater than zero were classified as exposed, whereas grains with Free Surface% equal to zero were classified as enclosed.

Particle locking complexity was characterised by the number of mineral species contributing at least 1% of particle mass. Particles were classified according to whether they contained one, two, three or four or more mineral species. The corresponding proportions were calculated using particle-mass weighting. Grain morphology was assessed using MLA's aspect ratio and angularity descriptors, following the general image-analysis approach described by Dumm and Hogg (1991).

The major mineral groups considered in the analysis were chromite, orthopyroxene, clinopyroxene, and plagioclase, consistent with the mineral groups identifiable using the

textural quantification framework of Nke et al. (2026). Hydrous-silicate alteration phases, comprising chlorite, talc, and mica, were also included in the analysis.

2.5. Statistical analysis

Associations between candidate sample-level descriptors and t_{10} were examined using Spearman's rank correlation. This non-parametric method was selected to assess monotonic associations without assuming a linear relationship or normally distributed variables. It was considered appropriate for the small sample set (n = 32), with careful attention to the resulting correlation estimates and significance tests, given the limited sample size. Leave-one-out sensitivity analysis was used to assess whether observed associations were strongly influenced by any individual sample.

The analysis also compared MLA-derived measurements across progeny size fractions and examined grain-shape differences between exposed and enclosed grains. Where appropriate, patterns were evaluated separately by sample and mineral group.

Given the 32-sample dataset, the number of candidate descriptors examined, and the absence of an independent validation set, the statistical analyses were considered exploratory. Statistical significance and leave-one-out sensitivity analysis were not interpreted as substitutes for independent validation or as evidence of predictive performance.

3. RESULTS

3.1. Quantified texture classification framework

The fixed K-means motif dictionary identified four recurring local textural motifs: massive, coarse-minor phase, convoluted intergrowth, and fine-aligned, as defined by the established textural quantification framework (Nke et al., 2026). The dictionary was applied to all 240 pieces of chromitite, including 70 held-out pieces excluded from fitting, and all were successfully classified without any being flagged as unclassifiable. All four motifs occurred in each ore layer and in every drillhole were represented by at least two samples (Table 1). Their proportions varied across layers and drillholes: the massive motif dominated MG3 (mean fraction 0.64), whereas UG1 showed more even proportions of the massive, coarse-minor phase, and convoluted-intergrowth motifs (0.29–0.30 each). The fine-aligned motif was consistently the least abundant (mean fractions 0.06–0.12). Variation between drillholes within the same layer was also observed, but the motif proportions did not indicate distinct drillhole-specific textural groups.

For descriptive purposes, a dominant-motif rule was also used to assign pieces to discrete sample classes. Pieces with a dominant motif fraction greater than 0.5 were assigned to that motif class, with subtyping based on the dominant mineral resolved by NNLS; the remaining pieces were classified as mixed but further distinguished based on their two largest motif fractions. This rule produced 13 classes across the dataset. The most frequent were mixed coarse-minor phase–convoluted intergrowth (61 pieces), massive chromite (50), and mixed coarse-minor phase–massive (44).

Table 1. *Mean motif area-fraction proportions by ore layer and drillhole on the complete 240 pieces dataset (H1–9 are used here simply to emphasize different drill holes)*.

Layer	Drillhole	n	Massive	Coarse-minor phase	Convoluted intergrowth	Fine-aligned
MG1	**(layer mean)**	**23**	**0.43**	**0.24**	**0.21**	**0.12**
MG1	MG1-H1	1	0.16	0.46	0.24	0.13
MG1	MG1-H2	4	0.10	0.27	0.42	0.21
MG1	MG1-H3	1	0.45	0.19	0.26	0.10
MG1	MG1-H4	1	0.13	0.48	0.19	0.21
MG1	MG1-H5	7	0.69	0.07	0.16	0.08
MG1	MG1-H6	2	0.33	0.31	0.28	0.08
MG1	MG1-H7	7	0.47	0.29	0.12	0.12
MG3	**(layer mean)**	**49**	**0.64**	**0.13**	**0.17**	**0.06**
MG3	MG3-H1	15	0.71	0.12	0.12	0.04
MG3	MG3-H2	13	0.70	0.14	0.10	0.05
MG3	MG3-H3	21	0.56	0.13	0.24	0.07
UG1	**(layer mean)**	**168**	**0.29**	**0.29**	**0.30**	**0.12**
UG1	UG1-H1	16	0.12	0.31	0.43	0.14
UG1	UG1-H2	18	0.22	0.28	0.34	0.16
UG1	UG1-H3	12	0.10	0.25	0.44	0.21
UG1	UG1-H4	11	0.21	0.29	0.35	0.16
UG1	UG1-H5	5	0.24	0.40	0.22	0.14
UG1	UG1-H6	19	0.30	0.26	0.33	0.11
UG1	UG1-H7	16	0.36	0.29	0.24	0.10
UG1	UG1-H8	41	0.39	0.27	0.25	0.09
UG1	UG1-H9	30	0.39	0.31	0.22	0.08

3.2. Comminution progeny selection for MLA

The t_{10} breakage response was measured for 32 pieces subjected to dropweight testing at a consistent applied specific energy of 1.00 kWh/t, spanning a range of 61.4–83.7% (Table 2). Under the dominant-motif classification described in Section 3.1, these 32 pieces resolved into four sample classes: massive chromite accounted for 21 of 32 pieces, with the

remainder classified as convoluted-intergrowth chromite (4) or one of two mixed classes (7 combined).

***Table 2**. Measured t_{10} values for all 32 pieces subjected to dropweight testing, ordered by decreasing t_{10}.*

Sample	t_{10} (%)	Sample	t_{10} (%)
MG3-1	83.7	MG3-17	72.1
MG3-2	82.6	MG3-18	71.7
MG3-3	80.3	MG3-19	71.6
MG3-4	80.1	MG3-20	71.4
MG3-5	79.6	MG3-21	70.6
MG3-6	79.0	MG3-22	70.5
MG3-7	78.8	MG3-23	70.3
MG3-8	78.3	MG3-24	70.2
MG3-9	76.5	MG3-25	69.3
MG3-10	76.1	MG3-26	68.8
MG3-11	75.4	MG3-27	68.4
MG3-12	75.3	MG3-28	66.6
MG3-13	73.8	MG3-29	63.6
MG3-14	73.7	MG3-30	62.9
MG3-15	73.2	MG3-31	61.6
MG3-16	72.1	MG3-32	61.4

3.3. Textural and mineralogical composition of the selected samples

The high- and low-t_{10} sample groups showed some overlap in motif proportions and derived textural classes (Figure 2). Both groups included samples dominated by the massive motif as well as samples with more mixed textural compositions. Across all 32 samples, the coarse-minor-phase motif showed the strongest association with t_{10} (Spearman's $\rho = -0.34$, $p = 0.059$, $n = 32$), indicating a tendency for samples with higher proportions of this motif to have lower t_{10} values. This pattern may be related to differences in silicate content, although this requires further investigation. The massive ($\rho = 0.13$, $p = 0.49$), convoluted-intergrowth ($\rho = -0.02$, $p = 0.91$), and fine-aligned ($\rho = -0.15$, $p = 0.42$) motifs showed no clear associations with t_{10}. Overall, the motif proportions provided limited separation of the high- and low- t_{10} groups and showed no statistically significant association with t_{10} across the full dataset.

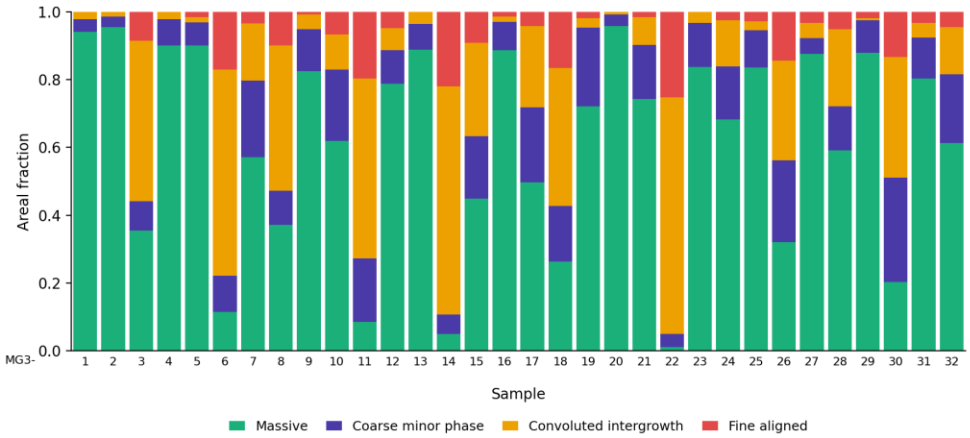

***Figure 2**. Motif area-fraction composition of all 32 t_{10}-tested MG3 pieces (Table 2), ordered by decreasing t_{10} (left to right, sample numbers as in Table 2).*

The relationship between bulk silicate content and t_{10} was examined across all 32 t_{10}-tested samples. Bulk silicate content was defined as the combined NNLS-resolved area percentages of orthopyroxene (OPX), clinopyroxene (CPX), and plagioclase, excluding the alteration silicates chlorite, talc, and mica (Figure 3). Because this measure was derived from the full micro-XRF map of each sample, it represents whole-piece composition rather than mineral composition within individual MLA progeny size fractions.

Across all 32 samples, bulk silicate content showed a weak, non-significant association with t_{10} (Spearman's $\rho = -0.13$, $p = 0.49$, $n = 32$), which remained weak under leave-one-out analysis ($\rho = -0.17$ to -0.04; all $p \geq 0.35$). A comparison of samples at the extremes of the t_{10} range showed a suggestive difference. The four highest-t_{10} samples (80.1–83.7%) were uniformly silicate-poor (0.0–2.4%; mean 0.6%), whereas the eight lowest-t_{10} samples (61.4–69.3%) had a wider range of silicate contents (0.2–25.6%; mean 5.7%). This difference was not statistically significant (Mann–Whitney $U = 6$, $p = 0.11$).

Overall, bulk silicate content alone did not explain the variation in t_{10} across the 32 samples. Although the highest-t_{10} samples were uniformly silicate-poor, the lowest-t_{10} group also included samples with near-zero silicate content, and the difference between the extreme groups was not statistically significant. Bulk composition therefore provides an incomplete explanation of the observed breakage response. Differences in mineral grain size or the spatial arrangement of mineralogical regions may also be relevant, but these possibilities cannot be resolved from bulk modal composition alone. The following analyses therefore examine whether spatial descriptors and post-breakage MLA measurements provide complementary information.

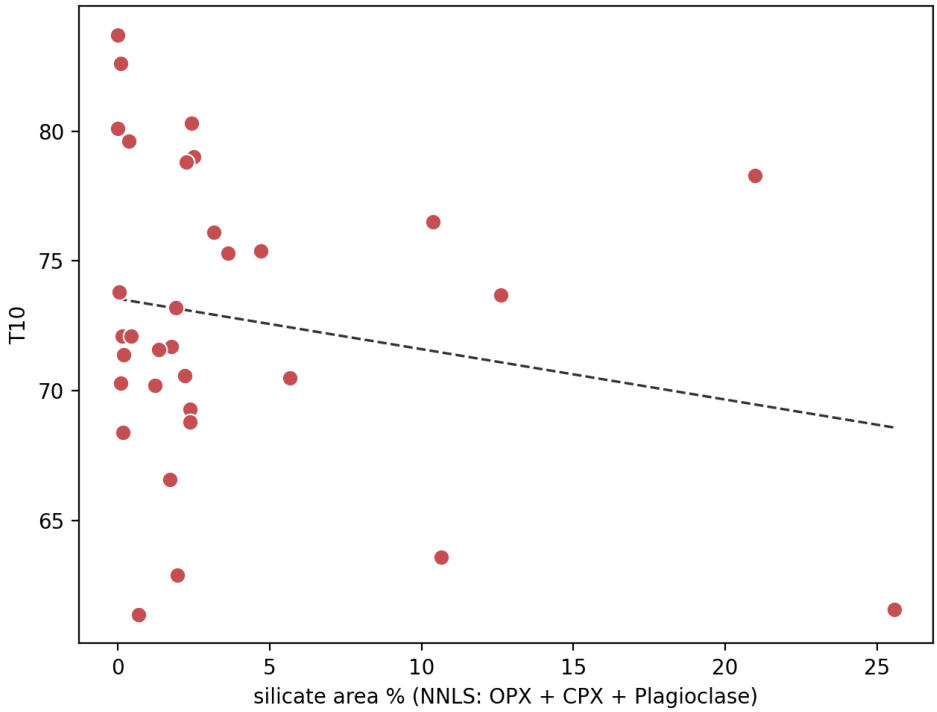

***Figure 3**. Bulk silicate proportion (NNLS: OPX + CPX + Plagioclase area %) vs t_{10} for all 32 t_{10}-tested MG3 pieces. Spearman rho=-0.13, p=0.49, n=32.*

3.4. MLA-derived liberation, grain size and particle locking

Across the five progeny size fractions, the proportion of grains exposed at particle boundaries increases with decreasing particle size. Liberation ranges from 57% to 86% in the coarsest fraction and exceeds 99.7% in the finest fraction (-212 µm) for each of the canonical mineral groups.

Clinopyroxene is the finest mineral in 32 of the 38 sample-by-fraction combinations (7 samples contained all 5 size fractions and 1 contained only 3) for which the relevant comparison was available. It also exhibited the lowest liberation in the coarser fractions. This pattern was consistent with the observed distribution and interstitial occurrence of clinopyroxene within the samples.

Chromite's relative liberation, calculated as the difference between its mean Free Surface% and that of the silicate minerals, was positively associated with the coarse-minor-phase motif fraction in three of the five size fractions (Spearman's $\rho = 0.81–0.86$, $p < 0.05$). The direction of the association was retained in seven of eight leave-one-out assessments. In one of several MLA-derived measurements screened for association with t_{10}, chromite's relative liberation was not associated with t_{10} in any fraction.

Hydrous-silicate alteration phases, including chlorite, talc and mica, were enriched in the finest fraction relative to the coarsest fraction in seven of the eight samples (Wilcoxon $p = 0.023$). This enrichment was not associated with t_{10} (Spearman's $\rho = 0.14$, $p = 0.74$).

Mineral locking complexity showed the expected relationship with progeny size. The proportion of monomineralic particles increased from approximately zero in the coarsest fraction to 65–90% in the finest fraction. However, the proportions of mono-, binary-, ternary- and quaternary-or-higher mineral assemblages did not show significant associations with t_{10} within individual size fractions.

Overall, the MLA-derived liberation, grain-size and locking-complexity measurements described changes associated with progeny size but did not individually explain the measured differences in t_{10} among the eight selected samples.

3.5. Other textural measurements and spatial descriptors

Among the additional spatial descriptors, the area-weighted textural complexity descriptor showed a negative association with t_{10} in the eight samples selected for MLA analysis (Spearman's $\rho = -0.83$, $p = 0.010$, $n = 8$; Table 3; Figure 4). The association remained statistically significant in all leave-one-out analyses ($p = 0.014$–0.036).

The descriptor was then calculated for all 32 t_{10}-tested MG3 samples because it was derived from the micro-XRF maps and did not require MLA data. The association remained negative but was weaker (Spearman's $\rho = -0.38$, $p = 0.030$, $n = 32$). In leave-one-out analyses, the association remained statistically significant for 29 of the 32 subsets; significance was lost when any one of the three highest- t_{10} samples (83.7%, 82.6% and 80.1%) was excluded. This indicates that the association was partly influenced by the highest-t_{10} observations.

In the eight-sample subset, the area-weighted textural complexity values ranged from 1.28 to 9.49 (median 3.53). Five candidate spatial measures were examined without correction for multiple comparisons. Taken together, these results identify textural complexity as a candidate descriptor that may capture variation associated with t_{10} beyond that represented by motif proportions. However, the selected sample set, sensitivity to high- t_{10} observations and absence of independent validation mean that this association should be treated as exploratory.

***Table 3**. Summary statistics for spatial descriptors derived from micro-XRF maps and their associations with t_{10}*

Sample	t_{10} (%)	No. of regions	Largest region fraction	Median region fraction	Weighted Mean		
					Textural complexity	Connectivity ratio	Clark Evans ratio
MG3-1	83.7	1	1	1	1.28	1	1
MG3-2	82.6	2	1.00	0.50	1.52	1.00	1.17
MG3-3	80.3	3	0.79	0.19	2.73	0.85	2.35
MG3-4	80.1	1	1	1	1.28	1	1
MG3-5	79.6	2	0.99	0.5	2.05	0.99	1.10
MG3-6	79	2	0.75	0.5	3.36	0.82	1.10
MG3-7	78.8	2	0.94	0.5	9.92	0.95	1.21
MG3-8	78.3	3	0.63	0.36	3.77	0.66	1.74
MG3-9	76.5	2	0.98	0.5	2.91	0.99	1.09
MG3-10	76.1	2	0.92	0.5	11.17	0.94	1.27
MG3-11	75.4	3	0.83	0.11	6.44	0.90	2.10
MG3-12	75.3	2	0.91	0.5	3.33	0.95	1.88
MG3-13	73.8	2	1.00	0.5	1.80	1.00	1.05
MG3-14	73.7	4	0.59	0.17	2.43	0.67	2.16
MG3-15	73.2	3	0.87	0.08	6.33	0.90	0.85
MG3-16	72.1	2	0.98	0.5	1.74	0.99	1.13
MG3-17	72.1	2	0.96	0.5	6.86	0.96	1.20
MG3-18	71.7	3	0.85	0.13	12.28	0.90	2.21
MG3-19	71.6	2	0.95	0.5	3.46	0.96	2.14
MG3-20	71.4	2	1.00	0.5	1.33	1	1
MG3-21	70.6	2	0.94	0.5	3.91	0.97	1.25
MG3-22	70.5	3	0.74	0.20	41.64	0.78	1.56
MG3-23	70.3	2	0.99	0.5	1.90	0.99	1.14
MG3-24	70.2	2	0.96	0.5	7.03	0.97	1.16
MG3-25	69.3	2	0.94	0.5	4.59	0.97	1.38
MG3-26	68.8	3	0.84	0.09	23.49	0.87	1.44
MG3-27	68.4	2	0.98	0.5	1.71	0.99	1.14
MG3-28	66.6	3	0.93	0.05	7.49	0.96	1.45
MG3-29	63.6	2	0.97	0.5	3.30	0.98	1.24
MG3-30	62.9	3	0.83	0.14	9.48	0.87	2.15
MG3-31	61.6	2	0.72	0.5	3.87	0.86	2.17
MG3-32	61.4	3	0.95	0.03	4.34	0.97	1.37

The spatial descriptors were calculated from micro-XRF maps acquired at a common native resolution of 20 μm. Five candidate spatial measures were examined without correction for multiple comparisons. In the eight-sample subset, samples contained one to three canonical textural regions, with the dominant region accounting for 63–100% of the mapped area (median 89%). The area-weighted textural complexity values ranged from

1.28 to 41.64 (median 3.41). These results suggest that the textural complexity descriptor may capture variation associated with t_{10} that is not represented by motif proportions alone. However, the small initial sample set, the dependence on a few high-t_{10} observations, the limited number of canonical textural regions per sample, and the absence of correction for multiple comparisons mean that this relationship should be treated as exploratory and requires independent validation.

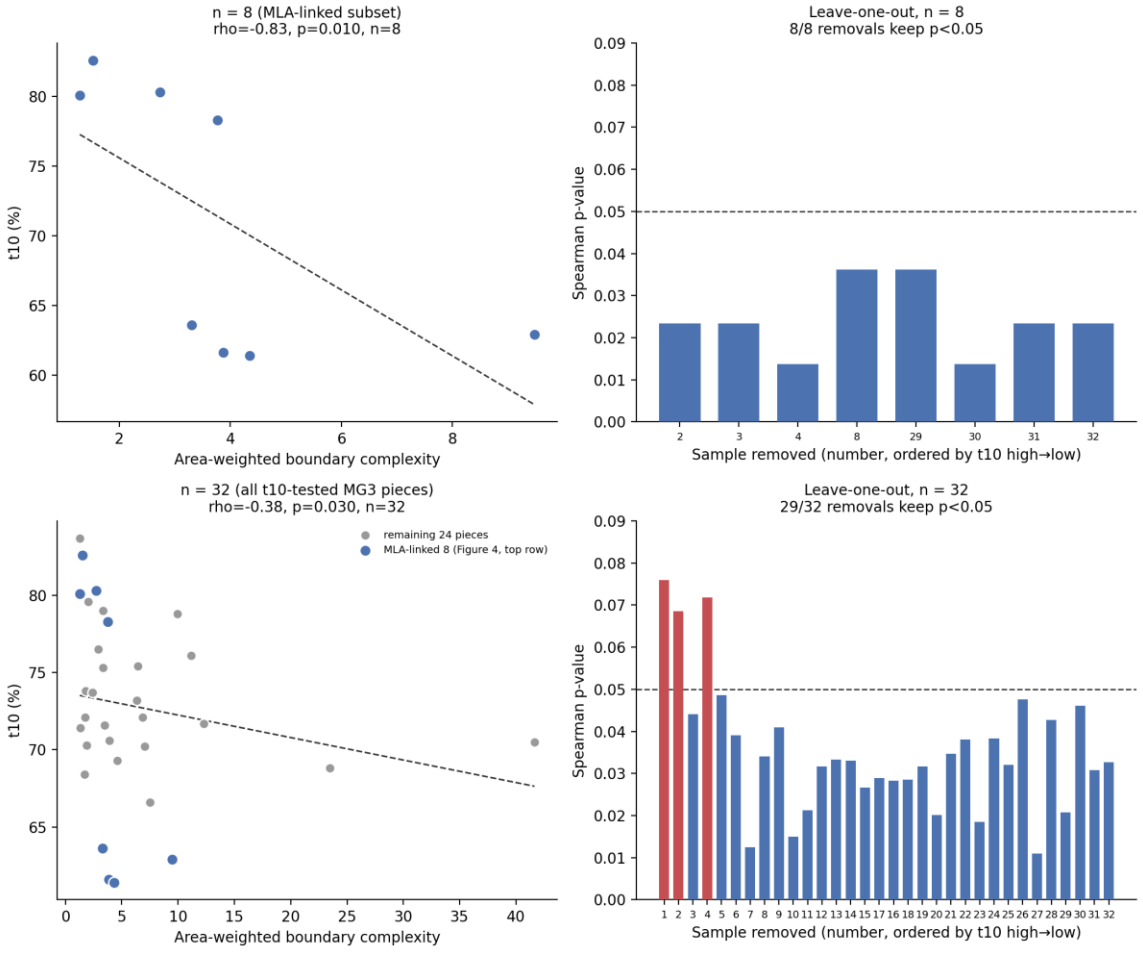

Figure 4. *Textural complexity vs. t_{10}, for the eight MLA-linked samples (top row) and all 32 t_{10}-tested MG3 pieces (bottom row, the same eight highlighted). Left column: area-weighted boundary complexity vs. t_{10}. Right column: leave-one-out robustness, the resulting Spearman p-value after removing each sample in turn; bars above the p = 0.05 line (red, bottom row) are the three highest-t_{10} pieces, whose removal is the only way the n = 32 association loses significance.*

3.5. Progeny grain morphology and particle-boundary exposure

The grain-level analysis included approximately 1.02 million grains from the canonical mineral groups. Grain angularity was compared between grains exposed at the external particle boundary and grains enclosed within particles, using the MLA Free Surface% descriptor to distinguish the two groups (Figure 5).

Exposed chromite grains were more angular than enclosed chromite grains. The relative increase in median angularity ranged from 41% to 109% across the three progeny size fractions with sufficient data, with $p < 0.001$ for the reported comparisons. The direction of this difference was observed in seven of the eight samples.

The silicate minerals showed the opposite pattern. Exposed orthopyroxene, clinopyroxene and plagioclase grains were less angular than enclosed grains, with relative differences ranging from −30% to −49%. This direction was observed in all eight samples for each silicate group. These results demonstrate systematic differences in the morphology of exposed and enclosed grains, but do not directly identify the fracture paths that produced the progeny.

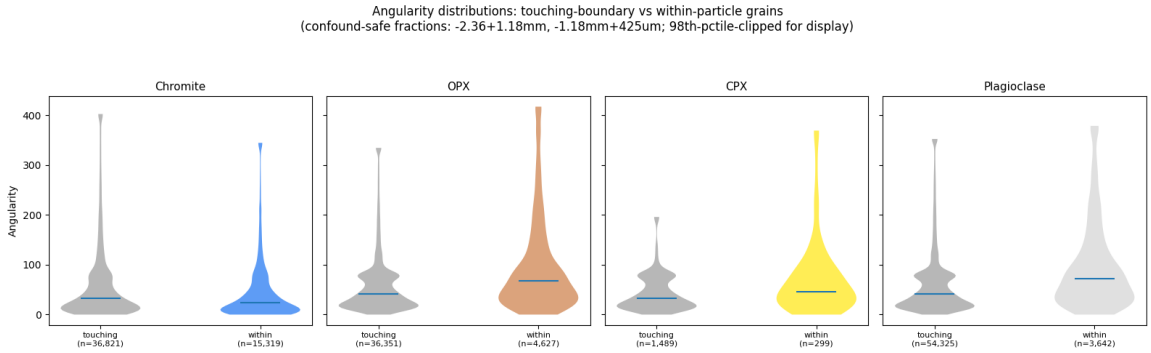

***Figure 5**. Grain population analysis from MLA-analysed progeny data.*

4. DISCUSSION

4.1. Motif proportions and the representation of whole-sample texture

Local motifs describe recurring textural patterns, while their proportions summarise the contribution of each pattern to a sample. These proportions do not necessarily capture the geometry, connectivity or spatial arrangement of the corresponding textural regions. Samples with similar motif proportions may therefore differ in their spatial organisation.

The additional spatial descriptors were investigated to explore whether such differences were associated with t_{10}. Of the candidate measures, the area-weighted textural complexity

descriptor showed the strongest association with t_{10}. This suggests that spatial information beyond motif proportions may be relevant to understanding variation in breakage response. However, the association was exploratory and does not establish that textural complexity is a general indicator or cause of breakage behaviour.

4.2. Complementary information from micro-XRF texture and MLA

The micro-XRF framework and MLA provide different representations of the samples. The micro-XRF workflow characterises chemically coherent textural regions and their spatial organisation, whereas MLA provides mineralogical and particle-level information on the post-breakage progeny.

A comparison of two samples illustrates the potential complementarity of these measurements. Samples MG3-4 and MG3-30 had similar NNLS-derived chromite contents of 100.0% and 98.0%, respectively. However, their reported textural complexity indices differed by a factor of 8.2 (1.28 versus 9.48), while their t_{10} values differed by approximately 17 percentage points (80.1 versus 62.9) (Table 3).

This comparison illustrates that similar estimated mineral-affinity proportions can coexist with differences in the spatial organisation of segmented regions. The spatial descriptor may therefore capture information that is not apparent from bulk compositional measures alone.

However, this single comparison does not establish that spatial textural complexity explains the t_{10} difference. The present study includes only eight selected samples, and MLA measurements were essential to characterising liberation, locking complexity and grain morphology.

The appropriate interpretation is that the two methods provide complementary types of information that may be useful in a broader process mineralogy workflow. Their relative contributions to explaining comminution response require evaluation using a larger, independently selected sample set.

4.3. Interpreting the association between textural complexity and t_{10}

The area-weighted textural complexity descriptor showed a negative association with t_{10} in the eight samples selected for MLA analysis. A negative association indicates that samples with higher descriptor values tended to have lower t_{10} values under the test conditions. The association remained statistically significant in leave-one-out analyses of this subset, but this sensitivity analysis does not establish that the relationship will generalise to other samples.

The association was weaker when the descriptor was calculated for all 32 t_{10}-tested MG3 samples, and statistical significance was lost when any one of the three highest-t_{10} samples was excluded. In addition, five candidate spatial measures were examined without correction for multiple comparisons. These factors limit the strength of the evidence and make independent validation essential.

The comparison between MG3-4 and MG3-30 illustrates why spatial descriptors may be useful alongside bulk composition: the samples had similar NNLS-derived chromite contents but differed in their reported textural complexity values and t_{10} responses. This example illustrates a potential benefit of measuring spatial organisation, but it does not demonstrate that textural complexity explains the difference in t_{10}. The most defensible interpretation is that the descriptor is a candidate for further testing, not an established predictor of comminution response.

4.4. Grain morphology and the hypothesis of textural-boundary-controlled breakage

The grain-shape analysis revealed contrasting patterns for chromite and silicate minerals. Exposed chromite grains were generally more angular than enclosed chromite grains, whereas exposed orthopyroxene, clinopyroxene and plagioclase grains were less angular than their enclosed counterparts. These differences were consistent across most or all samples.

The lower angularity of exposed silicate grains is consistent with a possible relationship between particle boundaries and the margins of rounded, silicate-rich interstitial clusters, including oikocrysts observed in the micro-XRF maps and hand specimens. If breakage follows the outer margins of these clusters, the resulting particle surfaces may expose less angular silicate profiles than would be expected if fractures cut across individual mineral grains. The contrasting pattern observed for chromite may also reflect differences in the geometry of mineral grains intersected by particle boundaries.

These observations are consistent with the hypothesis that breakage may be influenced by textural-domain boundaries, rather than exclusively by individual mineral grain boundaries. However, the grain-shape measurements were obtained from post-breakage MLA data and do not directly identify the fracture paths. The study did not include spatially registered pre-breakage texture maps, direct fracture observations or three-dimensional imaging. Furthermore, the MLA analysis cannot reliably distinguish boundaries between adjacent grains of the same mineral in all cases.

Consequently, the observed grain-shape patterns should not be interpreted as proof that fractures preferentially followed oikocryst margins or other textural-region boundaries. A direct test would require registered pre-breakage texture maps and post-breakage fracture observations, together with mapped mineral boundaries, to compare fracture alignment

with textural and mineral boundaries against an appropriate geometric reference. The current results motivate this investigation but do not establish a specific breakage mechanism.

4.5. Implications and limitations

The present study demonstrates the value of evaluating quantitative textural descriptors alongside post-breakage mineralogical measurements, while also showing the limitations of interpreting such associations using a small, selected dataset.

The four motif proportions provide a reproducible description of local textural patterns but did not individually distinguish the selected samples according to t_{10}. The additional spatial descriptor showed a stronger association with t_{10}, suggesting that the spatial organisation of textural regions merits further investigation. However, the observed relationship remains exploratory and has not been validated independently.

The MLA analysis characterised systematic changes in liberation and particle locking with progeny size, as well as contrasting grain-shape patterns between exposed and enclosed grains. These measurements did not individually provide a robust explanation of the differences in t_{10} among the selected samples.

Several limitations should be acknowledged. The analysis included eight samples, with one t_{10} derivation per sample. Consequently, the repeatability of the comminution measurements could not be assessed from the available data, and the generalisability of the observed relationships remains unknown. The textural descriptors were calculated from two-dimensional polished-section maps and cannot fully represent three-dimensional textural connectivity or fracture behaviour. In addition, the analysis considered multiple candidate descriptors, increasing the importance of independent validation.

Future work will prioritise replicate comminution measurements, a larger independent sample set — UG1 in particular, given its markedly more balanced motif distribution than MG3's massive-dominated texture and the substantial UG1 drill-core material already available — and multiple mapped sections per sample where feasible. Direct investigation of fracture mechanisms would require registered pre- and post-breakage imaging. These additions would help determine whether the spatial descriptors provide robust, transferable information about comminution response and whether that information can be linked to specific breakage mechanisms.

5. CONCLUSIONS

This study extended a micro-XRF-based framework for quantitative chromitite texture characterisation by examining additional spatial descriptors and comparing them with post-breakage MLA measurements from eight selected MG3 samples spanning a range of t_{10} values.

The four local textural motif proportions did not clearly distinguish samples by t_{10}. In contrast, the area-weighted textural complexity descriptor showed a negative association with t_{10} in the eight-sample subset, with a weaker association when extended to all 32 t_{10}-tested MG3 samples. This result suggests that spatial organisation may provide complementary information beyond motif proportions and bulk mineral composition. However, the association remains exploratory and requires independent validation.

MLA measurements characterised changes in liberation and particle locking across progeny size fractions but did not individually explain the differences in t_{10}. Grain angularity also differed systematically between exposed and enclosed grains: exposed chromite grains were generally more angular, whereas exposed silicate grains were less angular than their enclosed counterparts. The latter pattern is consistent with the hypothesis that breakage may follow the margins of silicate-rich textural domains, including oikocrysts, rather than exclusively following individual mineral grain boundaries. However, the available post-breakage measurements do not directly establish fracture paths or confirm this mechanism.

Overall, spatial textural descriptors may complement motif proportions and MLA-derived mineralogical measurements in the investigation of chromitite breakage. Further work should prioritise replicate comminution tests, a larger independently selected sample set, and registered pre- and post-breakage imaging to test whether textural complexity is a transferable indicator of t_{10} and whether fractures preferentially follow textural-domain boundaries.

ACKNOWLEDGEMENTS

This work was funded through Mintek's Science Vote research grant under work package MN33. The authors thank their industry partner for providing the chromitite drill core used in this study.

REFERENCES

Becker, M., Jardine, M.A., Miller, J.A. and Harris, M., 2016. X-ray Computed Tomography: A geometallurgical tool for 3D textural analysis of drill core. Proceedings of the Third AusIMM International Geometallurgy Conference, Perth, 15-16 June 2016, The Australasian Institute of Mining and Metallurgy, Melbourne.

Donskoi, E., Suthers, S.P., Campbell, J.J. and Raynlyn, T., 2008. Modelling and optimization of hydrocyclone for iron ore fines beneficiation—using optical image analysis and iron ore texture classification. International Journal of Mineral Processing, 87(3-4), 106-119

Dumm, T.F. and Hogg, R., 1991. An image processing algorithm for particle size characterization. Particle and Particle Systems Characterization, 8(1-4), 204-208.

Fandrich, R., Gu, Y., Burrows, D. and Moeller, K., 2007. Modern SEM-based mineral liberation analysis. International Journal of Mineral Processing, 84(1-4), 310-320.

Guntoro, P.I., Ghorbani, Y., Butcher, A.R., Kuva, J. and Rosenkranz, J., 2020. Textural Quantification and Classification of Drill Cores for Geometallurgy: Moving Toward 3D with X-ray Microcomputed Tomography (μCT) Natural Resources Research, 29(6), 3547-3565.

Koch, P.H., Lund, C. and Rosenkranz, J., 2019. Automated drill core mineralogical characterization method for texture classification and modal mineralogy estimation for geometallurgy. Minerals Engineering, 136, 99-109.

Lotter, N.O., Kowal, D.L., Tuzun, M.A., Whittaker, P.J. and Kormos, L., 2003. Sampling and flotation testing of Sudbury Basin drill core for process mineralogy modelling. Minerals Engineering, 16(9), 857-864.

Lund, C., Lamberg, P and Lindberg, T., 2015. Development of a geometallurgical framework to quantify mineral textures for process prediction. Minerals Engineering, 82, 61-77.

Månbro, C., Parian, M. and Rosenkranz, J., 2025. Exploring the role of ore texture in comminution and approaches to identify and promote non-random breakage. Minerals Engineering, *230*, 109405.

Nguyen, A., Tungpalan, K., Evans, C., Manlapig, E., Jackson, J., Nguyen, K. and Valenta, R., 2021. A method for rapid estimation of processing behaviour based on ore texture. Minerals Engineering, 171, 107111

Nke, A.Y., Chetty, D., Mashaba, D. and Thakurdin, Y., 2026. Quantitative Texture Classification of Bushveld Complex Chromitite from Micro-XRF Elemental Maps Using Unsupervised Learning. Proceedings of the 7th SAIMM Young Professionals Conference, Johannesburg, 29-30 September 2026, in prep.

Parian, M., Mwanga, A., Lamberg, P. and Rosenkranz, J., 2018. Ore texture breakage characterization and fragmentation into multiphase particles. Powder Technology, 327, 57-69.

Pérez-Barnuevo, L., Lévesque, S. and Bazin, C., 2018. Automated recognition of drill core textures: A geometallurgical tool for mineral processing prediction. Minerals Engineering, 118, 87-96.

Wills, B.A. and Finch, J.A., 2016. Wills' Mineral Processing Technology, 8th ed. Butterworth-Heinemann.